PERGAMON

International Journal of Heat and Mass Transfer 44 (2001) 3513–3528

International Journal of HEAT and MASS TRANSFER

www.elsevier.com/locate/ijhmt

Freezing dynamics of molten solder droplets impacting onto flat substrates in reduced gravity

S. Haferl [a], V. Butty [a], D. Poulikakos [a,*], J. Giannakouros [a], K. Boomsma [b,1], C.M. Megaridis [b], V. Nayagam [c]

[a] *Institute of Energy Technology, Laboratory of Thermodynamics in Emerging Technologies, Swiss Federal Institute of Technology, ETH Center, CH-8092 Zurich, Switzerland*

[b] *Department of Mechanical Engineering, University of Illinois at Chicago, 842 W. Taylor Street (M/C 251), Chicago, IL 60607, USA*

[c] *NASA John H. Glenn Research Center at Lewis Field, 21000 Brookpark Road, Cleveland, OH 44135, USA*

Received 18 May 2000; received in revised form 16 October 2000

Abstract

The axisymmetric impingement of solidifying molten solder droplets onto smooth metallic substrates in a reduced gravity environment is investigated numerically to provide basic information on the heat and fluid flow phenomena and determine the governing parameters of the process. The numerical predictions are also tested against experimental data. Millimeter-sized droplet impact events in reduced gravity are employed for scale up modeling of the impingement of picoliter size droplets of molten eutectic 63%Sn–37%Pb solder used in electronic chip packaging. The present article reports on both numerical (the main focus of the paper) as well as experimental work (for the purpose of verification). To this end, the employed numerical model considers the axisymmetric impact and subsequent solidification of an initially spherical, molten solder droplet on a flat, smooth, metallic substrate. The laminar Navier–Stokes equations, combined with the energy transport equations are solved simultaneously in the liquid region (melt) using a Lagrangian approach. In the solid (substrate and solidified droplet material) the heat conduction equation is solved. A time and space averaged (but phase dependent) model of the thermal contact resistance between the impacting droplet and the substrate is also incorporated in the formulation. The numerical model is solved using a Galerkin finite element method, where a deforming, adaptive triangular-element mesh is employed to accurately simulate the large-domain deformations caused by the spreading and recoiling of the impinging droplet fluid. The experimental work has been conducted in reduced gravity in the range 2×10^{-4} to 5×10^{-4} g with technically relevant impact velocities of ~ 0.2 m/s, in order to provide validation of the numerical predictions. These impact conditions correspond to $Re = \mathrm{O}(100)$, $We = \mathrm{O}(1)$, and $Fr = \mathrm{O}(10{,}000)$, $Ca = \mathrm{O}(0.001)$. Presentation of the numerical results in terms of the Froude and the Ohnesorge numbers aids their interpretation. Among the results that stand out is the formation of a large number of frozen ripples on the droplet surface as a result of the simultaneous manifestation of rapid fluid oscillations and solidification. Furthermore, a non-intuitive behavior of the solidification times is reported. Specifically, the dependence of the solidification time on the Froude number is not monotonic, but features a minimum for each distinct value of Ohnesorge number considered in this study. Despite the complexity of the phenomena, the numerical model captures well the main features of the experimental results. In addition, the model offers key insights on the influence of the Ohnesorge and Froude numbers on the dynamics of the solidification process. © 2001 Elsevier Science Ltd. All rights reserved.

1. Introduction

The study of phenomena related to surface impingement of liquid has been a matter of scientific investigations since the time of Lord Rayleigh [1]. These phenomena are relevant to a plethora of emerging

* Corresponding author. Tel.: +41-1-632-2738; fax: +41-1-632-1176.

E-mail address: poulikakos@ltnt.iet.mavt.ethz.ch (D. Poulikakos).

[1] Currently a doctoral candidate at the Laboratory of Thermodynamics in Emerging Technologies, Swiss Federal Institute of Technology, Zurich, Switzerland.

0017-9310/01/$ - see front matter © 2001 Elsevier Science Ltd. All rights reserved.
PII: S0017-9310(01)00015-1

Nomenclature

Bi	Biot number (dimensionless)
c	speed of sound in droplet fluid (m/s)
Ca	capillary number (dimensionless)
d	diameter (m)
Fr	Froude number (dimensionless)
g	gravitational acceleration (m/s^2)
h	heat transfer coefficient (W/m^2 K)
H	curvature (1/m)
$\overline{H}$	dimensionless curvature (dimensionless)
k	thermal conductivity (W/m K)
K	dimensionless thermal conductivity (dimensionless)
l	length (m)
L	latent heat of fusion (kJ/kg)
M	Mach number (dimensionless)
$\vec{n}$	normal direction (dimensionless)
Oh	Ohnesorge number (dimensionless)
Pe	Peclet number (dimensionless)
p	pressure (Pa)
P	dimensionless pressure (dimensionless)
Re	Reynolds number (dimensionless)
r	radial coordinate, radius (m)
R	dimensionless radial coordinate (dimensionless)
s	arc-length on the droplet free surface (m)
t	time (s)
$\vec{t}$	tangential direction (dimensionless)
T	temperature (K)
$\underline{\underline{T}}$	stress tensor (dimensionless)
u	radial velocity (m/s)
U	dimensionless radial velocity (dimensionless)
v	axial velocity (m/s)
V	dimensionless axial velocity (dimensionless)
We	Weber number (dimensionless)
z	axial coordinate (m)
Z	dimensionless axial coordinate (dimensionless)

Greek symbols

α	thermal diffusivity (m^2/s)
δ	Kronecker symbol (dimensionless)
ϵ	dimensionless Navier-slip coeffcient (dimensionless)
γ	surface tension (N/m)
μ	dynamic viscosity (kg/ms)
ρ	density (kg/m^3)
Θ	dimensionless temperature (dimensionless)
$\bar{\sigma}$	dimensionless stress tensor components (dimensionless)
τ	dimensionless time (dimensionless)
$\Delta\tau$	computational time-step (dimensionless)

Subscripts

0	initial
1	droplet
2	substrate
3	interface
amb	ambient
l	liquid
r	radial direction
s	solid
z	axial direction
θ	azimuthal direction

technologies, such as free form manufacturing [2], rapid prototyping [3] or solder jetting in the manufacturing of microelectronics [4]. In the latter process, molten solder droplets with diameter between 50 and 100 μm are jetted onto specific landing pads located on a chip or other electronic substrates. Relevant parameters of the solder jetting process include among others initial droplet shape, diameter, and velocity, and after impact with the substrate, spreading rate, substrate wettability, maximum spread diameter, ripple formation, and overall solidified droplet shape [5–7]. The latter is of special importance, since deviations in axial or radial extension can affect the reliability of the process [8].

A thorough understanding of the complex interweaved fluid dynamics, heat transfer and solidification phenomena is necessary to advance molten droplet deposition technologies. A number of important issues have to be borne in mind, in particular with relevance to deposition of molten microdroplets in general and to solder jetting in particular. Due to the length and time scales of the solder jetting technology (less than 100 μm and 100 μs) experimental measurements are scarcely able to resolve the underlying physics because of limitations of experimental resolution. Therefore, reliable numerical modeling can be a promising alternative for advancing the knowledge base in solder dispensing technologies. To exemplify related difficulties, there are no physical models available describing the advancement of the dynamic contact line, nor are there correlations available for the modeling of transient thermal contact resistance between the impinging droplet and the substrate. Both these phenomena affect the evolution of the impingement process and need to be handled (up to today heuristically) in numerical solutions [9], adding to the already formidable numerical difficulties of the modeling of the process. In order to increase experimental accessibility to the underlying physics, experiments on droplet impingement are being conducted in a reduced gravity environment

[10]. By virtue of thermofluidic similitude of characteristic non-dimensional groups [11], the above-mentioned time- and length-scales were scaled up to millimeter and millisecond resolution using millimeter-sized droplets in a reduced gravity environment. The present paper contains the companion numerical study of the same process and is validated against experimental results available to date. It is shown that the numerical simulations capture well the main features of the physics of the process and have the potential to improve our understanding of molten droplet deposition phenomena.

2. Experiments and the parametric domain

The parametric domain of the present numerical work is based on experimental results obtained from experiments conducted at the Drop Tower Facility at NASA Glenn Research Center at Lewis Field in Cleveland, Ohio. In the experiments, millimeter-sized molten solder droplets were ejected on demand in an inert (nitrogen) environment from a specially designed and fabricated droplet generator. The droplets impacted and solidified onto smooth metallic substrates. Prior to the experiments the employed substrates were grinded and polished to a mirror-like surface finish. Quantitative measures of the surface roughness using a profilometer yielded maximum deviations from the mean height of 1000 Å over a scanning length of 2 mm [12]. Reduced gravity conditions were obtained by dropping the entire experimental package in the above-mentioned drop tower. Approximately 2.2 s of reduced gravity at $\sim 0.05\%$ of earth's normal gravity (g) are attainable in this facility. The material ejected form the droplet generator was 63Sn/37Pb eutectic solder. The temperature of the ejected solder was 210°C (melting point is 183°C). The following property values were considered for the molten Sn/Pb solder alloy [9] at a nominal temperature of 210°C: surface tension $\gamma = 0.345$ N/m (in a nitrogen atmosphere), dynamic viscosity $\mu = 0.00262$ kg/ms, and latent heat of fusion $L = 42$ kJ/kg. Other relevant thermophysical property data of the employed solder as well as for stainless steel substrates are contained in Table 1.

The investigated parameter domain of the experiments including the diameter and velocity ranges is given in Table 2.

Table 1
Thermophysical properties of the materials used in the numerical simulations

Material	Density (kg/m^3)	Specific heat (J/kg K)	Thermal conductivity (W/m K)
63Sn/37Pb (liquid)	8218	238	25
63Sn/37Pb (solid)	8240	176	48
304 Stainless steel	7817	460	15 (at 100°C) 17 (at 200°C)

3. Numerical approach

The problem definition for the present discussion is schematically shown in Fig. 1. A liquid droplet originally of spherical shape moves downward in the gravitational direction towards a horizontal flat substrate. Just before impact, the droplet has a uniform temperature $T_{1,0}$, while the substrate is also at a uniform temperature $T_{2,0}$. The impact of the droplet on the surface is affected by a host of parameters, which includes the impact conditions and the thermophysical properties of the droplet and the substrate material. For the numerical solution we will follow a fractional step approach, in which the fluid mechanical and the thermal phenomena are advanced in consecutive substeps within the same time step. In that sense, we consider the two phenomena separately.

The mathematical model is based on the Navier–Stokes equations applied to the axisymmetric coordinate system shown in Fig. 1. Laminar flow of a constant property fluid is assumed, and the motion of the deforming free surface is simulated using the Lagrangian approach. The time-dependent density term in the continuity equation is retained, which becomes a pressure evolution equation by applying the artificial compressibility approach [13]. Non-dimensionalization was performed according to the following definitions:

$$R = \frac{r}{d_0}, \quad Z = \frac{z}{d_0}, \quad U = \frac{u}{v_0}, V = \frac{v}{v_0}, \quad \tau = \frac{t}{d_0/v_0},$$
$$P = \frac{p - p_{\mathrm{amb}}}{\rho v_0^2}, \quad \bar{\sigma}_{ij} = \left(\sigma_{ij} + \delta_{ij} p_0\right)/\rho v_0^2. \tag{1}$$

The dimensionless forms of the governing fluid mechanical equations are expressed as

Table 2
Ranges of the investigated parameter domain including velocity and diameter

Reynolds number	Froude number	Weber number	Velocity (m/s)	Diameter (mm)
574–1410	3806–36,745	0.66–4.5	0.15–0.43	0.97–1.24

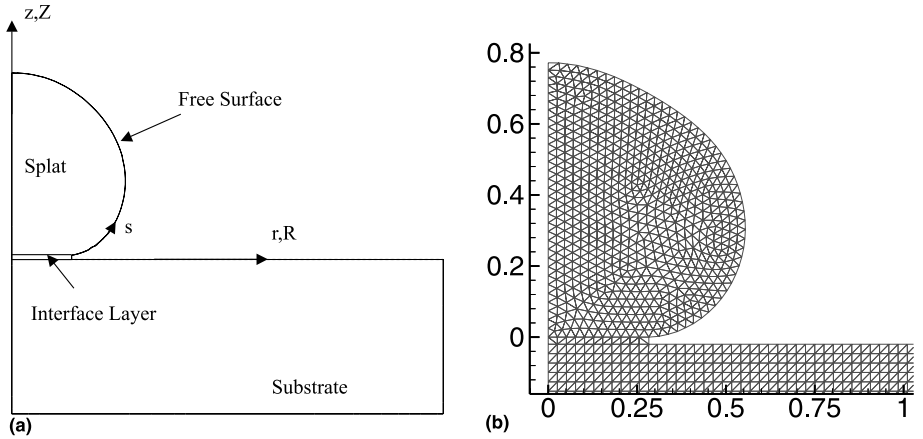

Fig. 1. (a) Schematic of the droplet impingement process defining the coordinate system, the arc-length, and the concept of the interfacial layer between the droplet and the substrate. (b) Example FEM-mesh of an impacting and spreading droplet. The substrate domain is only partially shown. The droplet region consists of 694 nodes and 1294 elements, respectively.

$$\frac{\partial P}{\partial \tau}+\frac{1}{M^2}\left(\frac{1}{R}\frac{\partial}{\partial R}(RU)+\frac{\partial V}{\partial Z}\right)=0, \tag{2}$$

$$\frac{\partial U}{\partial \tau}-\frac{1}{R}\frac{\partial}{\partial R}(R\bar{\sigma}_{rr})-\frac{\partial \bar{\sigma}_{rz}}{\partial Z}+\frac{\bar{\sigma}_{\theta\theta}}{R}=0, \tag{3}$$

$$\frac{\partial V}{\partial \tau}-\frac{1}{R}\frac{\partial}{\partial R}(R\bar{\sigma}_{rz})-\frac{\partial \bar{\sigma}_{zz}}{\partial Z}-\frac{1}{Fr}=0 \tag{4}$$

with the dimensionless stress components $\bar{\sigma}_{ij}$ given by

$$\begin{aligned}&\bar{\sigma}_{rr}=-P+\frac{2}{Re}\frac{\partial U}{\partial R}, \quad \bar{\sigma}_{zz}=-P+\frac{2}{Re}\frac{\partial V}{\partial Z},\\ &\bar{\sigma}_{\theta\theta}=-P+\frac{2}{Re}\frac{U}{R}, \quad \bar{\sigma}_{rz}=\frac{1}{Re}\left(\frac{\partial U}{\partial Z}+\frac{\partial V}{\partial R}\right).\end{aligned} \tag{5}$$

The Reynolds, Froude and Mach numbers are given, respectively, by

$$Re=\frac{\rho v_0 d_0}{\mu}, \quad Fr=\frac{v_0^2}{d_0 g}, \quad M=\frac{v_0}{c}. \tag{6}$$

The dimensionless initial and boundary conditions have the following form:

$$\begin{aligned}&U=0, \quad V=-1, \quad P=\frac{2}{We}, \quad \tau=0, \ U=0,\\ &\frac{\partial V}{\partial R}=0, \quad R=0, \quad U=V=0, \quad Z=0\end{aligned} \tag{7}$$

and at the free surface

$$\bar{\sigma}_{rr}n_r+\bar{\sigma}_{rz}n_z=-2\frac{\bar{H}}{We}n_r, \quad \bar{\sigma}_{rz}n_r+\bar{\sigma}_{zz}n_z=-2\frac{\bar{H}}{We}n_z. \tag{8}$$

In the above, We denotes the Weber number, defined as

$$We=\frac{\rho d_0 v_0^2}{\sigma} \tag{9}$$

and $\bar{H}=H/d_0$, where the dimensional mean curvature of the surface is defined as

$$H=\frac{r^2(r'z''-z'r'')+\left[(r')^2+(z')^2\right]rz'}{2r^2\left[(r')^2+(z')^2\right]^{3/2}}. \tag{10}$$

The primes in Eq. (10) indicate differentiation with respect to the arc length s of the free surface, as depicted in Fig. 1(a). In the above dimensionless equations, the hydrodynamic boundary condition at the wetting line was not introduced. This condition involves several interesting physical phenomena and constitutes always the object of modeling controversy. It is a well-known fact that, attempting to enforce purely fluid-dynamical (i.e., macroscopic) boundary conditions in the neighborhood of the contact line results in the non-physical appearance of infinite values for the local fluid-dynamical stresses. Common remedies involve the imposition of either a set slip velocity at the contact line or of a set value for the contact angle between the liquid surface and the substrate plane (two approaches which are more-or-less arbitrary, but which have proven to remove the singularity problem in actual simulations). Our approach here will be to impose a Navier-slip model of the form

$$\vec{n}\cdot\underline{\underline{T}}\cdot\vec{t}=\frac{1}{\varepsilon}\cdot\vec{u}\cdot\vec{t}, \tag{11}$$

where $\underline{\underline{T}}$ is the dynamic stress tensor, $\vec{n}$ and $\vec{t}$, respectively, the normal and tangent unit vectors to the substrate, u the radial velocity and ϵ the Navier-slip length taken to be of the order of 10^{-3} [14].

As mentioned above, the thermal phenomena are considered to closely follow the evolution of fluid mechanics in a fractional-step approach. The Lagrangian formulation is also used to construct the mathematical model for the conjugate heat transfer process in the droplet domain as well as in the substrate. The relevant

non-dimensional energy conservation equations, initial and matching conditions are expressed below.

The energy equation in the droplet ($i = 1$) and the substrate ($i = 2$) takes the form

$$\frac{\partial \Theta_i}{\partial \tau} = \frac{1}{Pe_i}\left[\frac{1}{R}\frac{\partial}{\partial R}\left(R\frac{\partial \Theta_i}{\partial R}\right) + \frac{\partial^2 \Theta_i}{\partial Z^2}\right], \tag{12}$$

where the dimensionless temperature is

$$\Theta_i = \frac{T_i - \min(T_{1,0}, T_{2,0})}{|T_{1,0} - T_{2,0}|}, \quad i = 1, 2 \tag{13}$$

and the Peclet number

$$Pe_i = \frac{d_0 v_0}{\alpha_i}, \quad i = 1, 2. \tag{14}$$

In Eq. (14), α_i represents the thermal diffusivities of the different regions ($i = 1$ droplet; $i = 2$ substrate).

Initial conditions

$$\tau = 0: \ \Theta_1(R, Z, 0) = 1, \quad \Theta_2(R, Z, 0) = 0. \tag{15}$$

Boundary conditions at the droplet free surface and the substrate boundary surface

$$\frac{\partial \Theta_i}{\partial R} n_r + \frac{\partial \Theta_i}{\partial Z} n_z = 0, \quad i = 1, 2. \tag{16}$$

Thermal contact resistance between the splat and the substrate is modeled by a thin layer of arbitrary thickness, l_3, which connects the two regions. This layer is assigned zero heat capacity and experiences only axial conduction. The effective layer axial thermal conductivity, $K_{Z,3}$, is related to the contact heat transfer coefficient in non-dimensional form by

$$K_{Z,3} = Bi\frac{l_3}{d_0}. \tag{17}$$

The Biot number at the interface is

$$Bi = \frac{h_3 d_0}{k_1}, \tag{18}$$

where h_3 is the unknown heat transfer coefficient between the droplet and the substrate region.

The resulting dimensionless heat conduction equation for the interface layer ($i = 3$) is

$$\frac{\partial \Theta_i}{\partial \tau} = \frac{2}{Pe_i}\left[\frac{\partial^2 \Theta_i}{\partial Z^2}\right], \quad i = 3. \tag{19}$$

Since the energy equations for the droplet fluid and the substrate have exactly the same form in a Lagrangian formulation, the fluid region can be combined with the solid region and the energy equations can be solved in this combined region following the same numerical procedure. The convective effect on the transfer of energy in the splat is implicit in the Lagrangian formulation. The movement of fluid particles in the deforming droplet represents this convective effect.

Numerical modeling of the solidification process is accomplished by utilizing the 'exact specific heat method' proposed by Bushko and Grosse [15]. In this approach the specific heat of the droplet material is temperature dependent, and is defined as

$$c_p(T) = \{c_{p,s}(T < T_m), c_{p,l}(T > T_m)\} + L\delta(T - T_m). \tag{20}$$

The Dirac function δ vanishes everywhere except at the melting temperature $T = T_m$. This formulation allows an exact integration of the capacitance terms in a Galerkin finite element formulation when linear triangle elements are employed. The advantage of this approach is that it conserves energy very accurately as the droplet solidifies.

Many features of the above-mentioned approach are similar to that used by Waldvogel et al. [8,16], with the significant exception that all the mesh-regenerating, and the surface-reconstruction approach are fundamentally different. Whereas Waldvogel et al. [8,16] used an advancing front algorithm with remeshing, we opted for a more refined commercially available tool (Hypermesh®, marketed by Altair Engineering) using Delaunay tesselation given the surface distribution of points. We verified improved stability, as well as enhanced quality of the surface features, possibly both owing to the fact that the resultant meshes in the splat interior turned out to be almost equidistributed, which means that discretization errors of the finite element model were essentially balanced throughout the numerical domain. Hence, no concentrated numerical errors could cause a local instability. A representative example of a mesh of an impacting droplet is shown in Fig. 1(b). The mesh shown in Fig. 1(b) consists of 694 nodes and 1294 elements in the droplet domain. The substrate domain, which is only partially shown in Fig. 1(b), consists of 2184 nodes and 4181 elements, respectively.

The Bach–Hassager iterative scheme [17] (involving a mesh-following algorithm coupled with backward-Euler time-stepping) was used for the fluid-mechanical fractional step. In the subsequent energy transfer substep, the thermal equations were discretized on the resulting finite element mesh using the same velocity values determined at the end of the fluid-mechanical substep. The curve representing the solidification front was gleaned as the locus of points inside the droplet having temperature equal to the melting temperature of the solder phase, and was calculated taking also into account the local velocity field. Time-stepping for the energy fractional step was implemented with a Crank–Nicholson scheme.

4. Results and discussion

4.1. Impact conditions and corresponding dimensionless numbers

The dimensionless groups mentioned in the foregoing section represent the collective effect of the physical and geometrical parameters on the fluid-dynamical aspect of the problem. In droplet impact studies at low Weber numbers the Ohnesorge number, *Oh*, often appears, scaling the two foremost important dimensionless groups in the droplet impact process [18], the Weber and Reynolds number, as follows

$$Oh = \frac{\sqrt{We}}{Re} = \frac{\mu}{\sqrt{\rho d_0 \gamma}}. \tag{21}$$

In the present study, the independent groups are taken to be *Oh* and *Fr*. Reduced gravity conditions are simulated by defining the gravity constant in the expression for Froude as being of in the range 10^{-4} to 10^{-3} m/s^2. Based on the dimensionless numbers and the velocity and diameter ranges for the experiments stated in Table 2, the array of cases solved numerically is listed in Table 3.

According to experimental data [10] the measured gravity level lies in the range from 2–5 $\times 10^{-4}$ g. The Froude numbers given in Table 3 are calculated using the reduced gravity value of (2×10^{-4} g). Furthermore, the cases in Table 3 are sorted by constant Ohnesorge number, corresponding to constant diameter. As in the experiments, the range of diameters considered in the modeling is from 0.9 to 1.2 mm, and the range of velocities from 0.1 to 0.4 m/s.

Further important dimensionless numbers relevant for the numerical simulation of molten droplet impact are the Stefan number and the Prandtl number defined as follows:

$$Ste = \frac{c_{p,l}(T_m - T_{2,0})}{L}, \tag{22}$$

$$Pr = \frac{\mu_l c_{p,l}}{k_l}. \tag{23}$$

For the thermal regime considered in this work, the Stefan and Prandtl number are assumed to be constant, which can be deemed as justified since there exist only small changes in the temperature. The values are

$$Ste = 0.895 \quad \text{and} \quad Pr = 0.025. \tag{24}$$

4.2. Determination of thermal contact resistance

In the modeling of molten droplet impact, cooling and subsequent solidification, the thermal contact re-

Table 3
Impact conditions and corresponding dimensionless groups for the investigated cases

Case	d_0 (mm)	v_0 (m/s)	*Re*	*We*	*Fr*	*Oh*
1	0.9	0.100	282.298	0.214	5555.556	0.00164
2	0.9	0.150	423.447	0.482	12,500.000	0.00164
3	0.9	0.200	564.595	0.858	22,222.222	0.00164
4	0.9	0.250	705.744	1.340	34,722.222	0.00164
5	0.9	0.300	846.893	1.929	50,000.000	0.00164
6	0.9	0.350	988.042	2.626	68,055.556	0.00164
7	0.9	0.400	1129.191	3.430	88,888.889	0.00164
8	1.0	0.100	313.664	0.238	5000.000	0.00156
9	1.0	0.150	470.496	0.536	11,250.000	0.00156
10	1.0	0.200	627.328	0.953	20,000.000	0.00156
11	1.0	0.250	784.160	1.489	31,250.000	0.00156
12	1.0	0.300	940.992	2.144	45,000.000	0.00156
13	1.0	0.350	1097.824	2.918	61,250.000	0.00156
14	1.0	0.400	1254.656	3.811	80,000.000	0.00156
15	1.1	0.150	517.546	0.590	10,227.273	0.00148
16	1.1	0.200	690.061	1.048	18,181.818	0.00148
17	1.1	0.300	1035.092	2.358	40,909.091	0.00148
18	1.1	0.350	1207.607	3.210	55,681.818	0.00148
19	1.1	0.400	1380.122	4.192	72,727.273	0.00148
20	1.2	0.100	376.397	0.286	4166.667	0.00142
21	1.2	0.150	564.595	0.643	9375.000	0.00142
22	1.2	0.200	752.794	1.143	16,666.667	0.00142
23	1.2	0.250	940.992	1.787	26,041.667	0.00142
24	1.2	0.300	1129.191	2.573	37,500.000	0.00142
25	1.2	0.350	1317.389	3.502	51,041.667	0.00142
26	1.2	0.400	1505.588	4.573	66,666.667	0.00142

sistance between the hot droplet and the cool substrate plays an important role when accurate modeling is pursued. With the exception of [9], no complete data have been published to date determining the value of the thermal contact resistance in the parametric domain of solder jetting. Experiments employing millimeter-sized droplets have shown a time-dependence of the contact resistance during impact, solidification, and post-solidification cooling [19–23]. Moreover, Liu et al. [21] and Wang and Matthys [19] reported that the thermal contact resistance can increase by an order of magnitude during solidification. Xiong et al. [9] reported a distinct influence of the thermal contact resistance on important process parameters such as contact area, height and overall shape of the solidified droplet. They assumed constant values for the thermal contact resistance and matched experimentally obtained droplet shapes with numerically-obtained shapes. In order to take the effect of solidification on thermal contact resistance into account, they used two different values for the contact resistance (pre-solidification or post-solidification). In the current work the same approach of Xiong et al. [9] was followed. A large number of numerical results with varying values of thermal contact resistance were produced using the same thermophysical properties, Reynolds, Weber, and Froude numbers as in the experiments (Table 2). Comparing the numerical shapes (Fig. 2) with the experimental one (Fig. 3), allowed the determination of a set of values for the thermal contact resistance. Fig. 2 depicts four different numerically obtained shapes of solidified droplets, which impacted with identical fluid-mechanical and thermal conditions but experienced different thermal contact resistances. As can be seen by comparing Fig. 2(d) with Fig. 3, a good matching between the numerical and the experimental results could be obtained by using the following values:

$$Bi_l = 1.05, \quad Bi_s = 0.07, \\ h_{3,l} = 30\ \mathrm{kW/m^2\ K}, \quad h_{3,s} = 2\ \mathrm{kW/m^2\ K}, \tag{25}$$

where the subscripts l, s denote the liquid and solid phases, respectively, and h is the corresponding heat transfer coefficient. The values of the Biot numbers, and the heat transfer coefficients evaluated above for the present cases are withal comparable with the corresponding values evaluated in [9].

For simplicity and since the simulations were meant to capture the physics of the process, it was assumed that the determined set of values for the thermal contact resistance could be employed for all simulations in the chosen range of Reynolds, Weber, and Froude number (Table 3). Clearly, experimentally obtained transient thermal contact resistances will aid the agreement between the simulations and the experiments if used as input to the simulations. Unfortunately, such data require rather involved experiments and to the best of our knowledge are not currently available.

In addition to the determination of the thermal contact resistance, several calculations were carried out in order to assure the grid independence of the results. Grid independence of the results was obtained when using approximately 1100 triangular elements in the splat region, corresponding to approximately 600 nodes. The time step used in the simulations was $\Delta\tau = 2.5 \times 10^{-4}$. The computations were carried out on a desktop PC (600 MHz, Pentium III), where a typical run required approximately 24 CPU h to complete 40,000 time-steps.

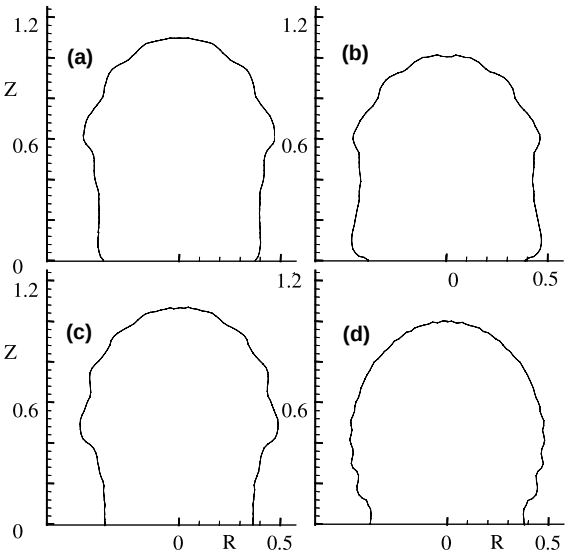

Fig. 2. Series of solidified solder bump shapes as predicted by the model for different values of thermal contact resistance for the following non-dimensional impact conditions: $Re = 739$, $We = 1.282$, $Fr = 25{,}240$, $T_0 = 208°C$, $T_{sub} = 25°C$. The corresponding Biot numbers are: (a) $Bi_l = 1.0$, $Bi_s = 0.5$; (b) $Bi_l = 1.5$, $Bi_s = 1.0$; (c) $Bi_l = 0.2$, $Bi_s = 0.2$; (d) $Bi_l = 1.05$, $Bi_s = 0.07$.

4.3. Comparison with experimental results

Part of the evaluation of the ability of the numerical code to capture the main features of the experimental results is to compare the *transient* visualization sequences obtained from experiments in the Drop Tower with numerical solutions. As can be seen for a typical case, the agreement of the fluid-mechanical evolution of the impingement process between the numerical results, Fig. 4, and the experimental results [10], Fig. 5, is very good. Both results correspond to the following set of dimensionless numbers: $Re = 739$; $We = 1.282$; $Fr = 25{,}240$. A slight tendency of overestimating axial dimensions in the numerical solution at the time-steps indicated in Fig. 4 is visible. In the observed outlines of

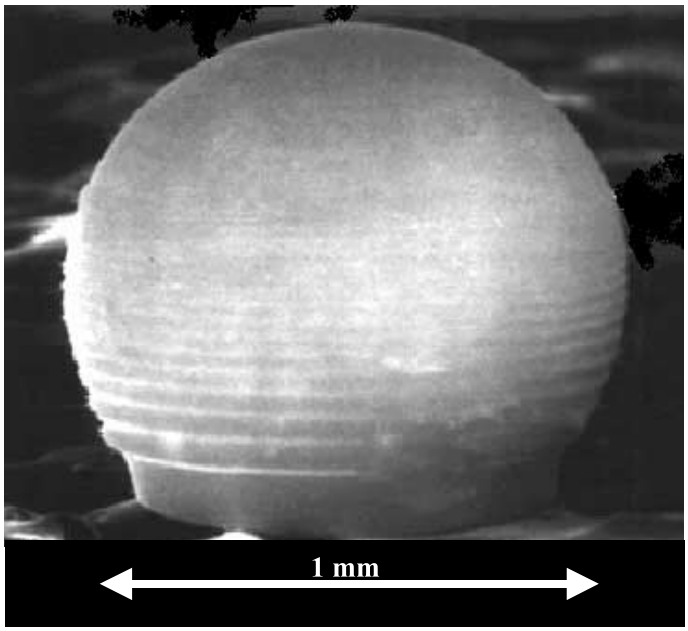

Fig. 3. Scanning electron micrograph of a molten solder droplet generated and solidified upon impact in reduced gravity. The droplet was positioned on an adhesive base (notice rough texture) to obtain this photograph. Impact conditions: $Re = 739$, $We = 1.282$, $Fr = 25{,}240$, $T_0 = 208°C$, $T_{sub} = 25°C$.

Fig. 5, not many small ripples can be identified near the top of the drop. These images have been processed using an edge finding algorithm to identify the droplet boundary. The inability to resolve the ripples is due to the insufficient resolution of the high-speed camera (KODAK RO Imager) used in the experiments [10]. However, the scanning electron micrograph shown in Fig. 3 for the solidified droplet of the experiment corresponding to Fig. 5, reveals that a plethora of ripples does exist (a direct result of the combined effect of droplet oscillations and freezing advancing from below) and that the numerical code captures very well its main features. These ripples are decreasing in size and increasing in frequency with increasing distance from the substrate as predicted by the numerical solution (Fig. 4). Furthermore, the time scales as well as the temporal advancement of the solidification process in the experiment agree well with the numerical predictions (compare Figs. 4 and 5). This includes the final solidification time, e.g., the time where the droplet mass has solidified entirely and no further fluid movement can be observed by means of the experimental visualization procedure. It is also worth clarifying that the ripples are the direct result of the droplet oscillation and the freezing from below process, as we have demonstrated in earlier work [8]. They are not due to capillary waves. This is why they do not appear in the liquid region (above the freezing front). This demonstrated important capability of the code adds confidence to the numerical investigation of the droplet impact/heat transfer/solidification process in the entire range of interest of the dimensionless groups.

4.4. Solidification during droplet impingement

The numerical results in this section focus primarily on the effects of impact velocity and droplet diameter, expressed as Froude and Ohnesorge number, respectively, on the solidification process. Therefore, all parameter variations pertain to initial impact velocity and diameter of the impinging droplets, as shown in Table 3. The baseline conditions are given by the thermophysical properties for solder and stainless steel 304 (Table 1), as well as the Biot numbers for the interfacial heat transfer determined in a preceding section. The initial temperatures are equal for all cases. The solder droplet impacts with an initial temperature of 208°C, whereas the substrate is initially at an ambient temperature of 25°C.

The results of all cases listed in Table 3, compiled in groups of constant Ohnesorge numbers, were selected to demonstrate the effects of the above-mentioned parameter variations on the solidification process. Fig. 6 presents a collective plot of solidification times for all Ohnesorge number considered. It reveals a non-intuitive trend concerning the final solidification times, t_{finish}. For constant Ohnesorge number, which for the cases investigated herein corresponds to constant droplet diameter, a distinct minimum in the final solidification times is

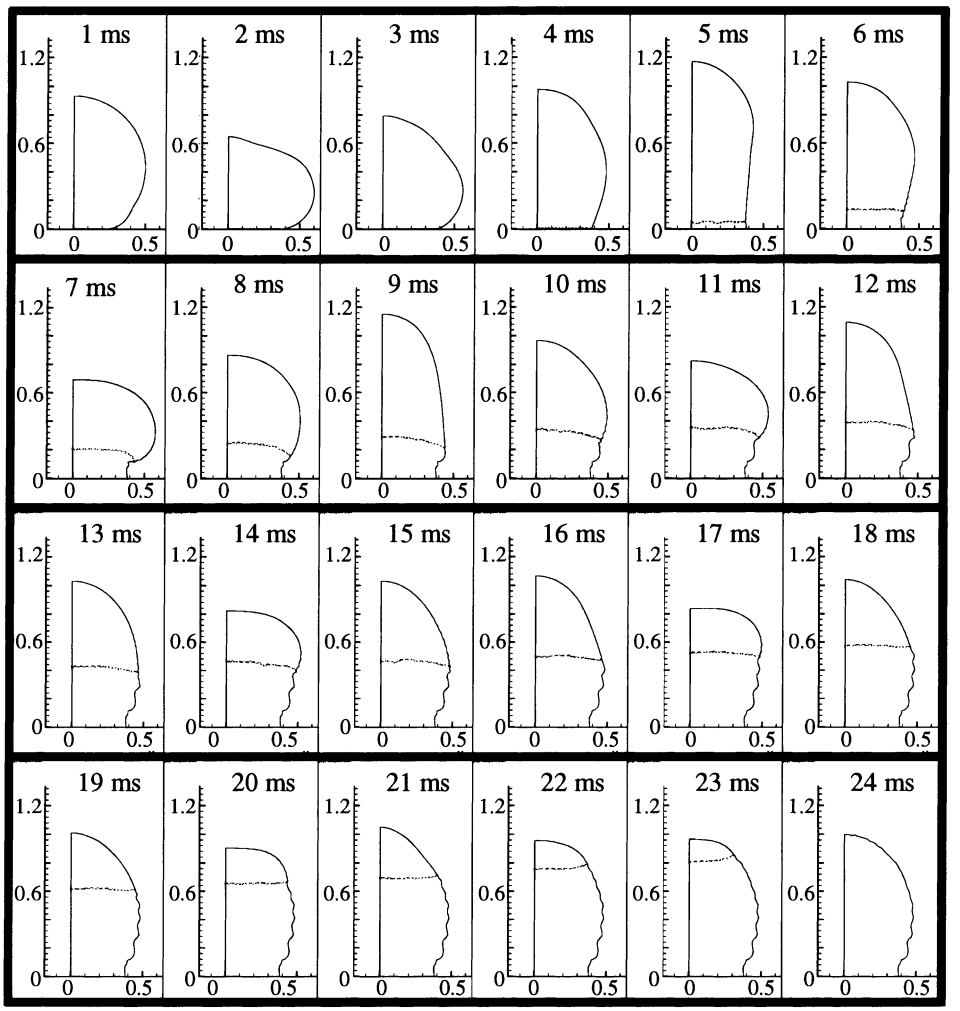

Fig. 4. Dynamics of the droplet impingement process. The non-dimensional impact parameters are: $Re = 739$, $We = 1.282$, $Fr = 25{,}240$. The corresponding impact temperatures are: $T_0 = 208°C$, $T_{sub} = 25°C$. The thin, advancing line within the droplet corresponds to the solidification front.

found within the Froude number regime of interest. In other words, in a group of identical droplets, the one that impacts with the highest velocity (more spreading and more contact area with the cold substrate) does not solidify the fastest. Indeed, as shown in Fig. 7, for higher Froude numbers, equivalent to higher impact velocities when the diameter (Oh) is held fixed, the dimensionless radius of the solidified contact area, x_{solid}, increases monotonically with increasing Froude for all Ohnesorge values. Furthermore, with decreasing Ohnesorge number (i.e., increasing diameter) the solidified droplet footprint radius x_{solid} is expected to increase at a fixed value of Froude number (Fig. 7). This result makes sense physically since the effect of inertia increases with increasing droplet diameter. On the other hand, as shown in Fig. 6, the solidification time behavior is more complex. An explanation for this behavior will be pursued subsequently in this section.

Fig. 8 presents the calculated temporal evolution of the droplet solid fraction for the chosen group of constant Ohnesorge number ($Oh = 0.00164$). The solidification behavior shows a practically linear dependence of the solid-fraction growth on time. The time of complete solidification can be thought of as dependent on two parameters: the initiation time of solidification and the slope of the linear curve in Fig. 8. The question arises as to which phenomena affect the two above mentioned parameters. A closer look at the initial stages of solidification reveals the existence of competing phenomena, affecting the efficiency with which the initial energy in combination with the latent heat can be removed from the droplet during freezing. It should be kept in mind

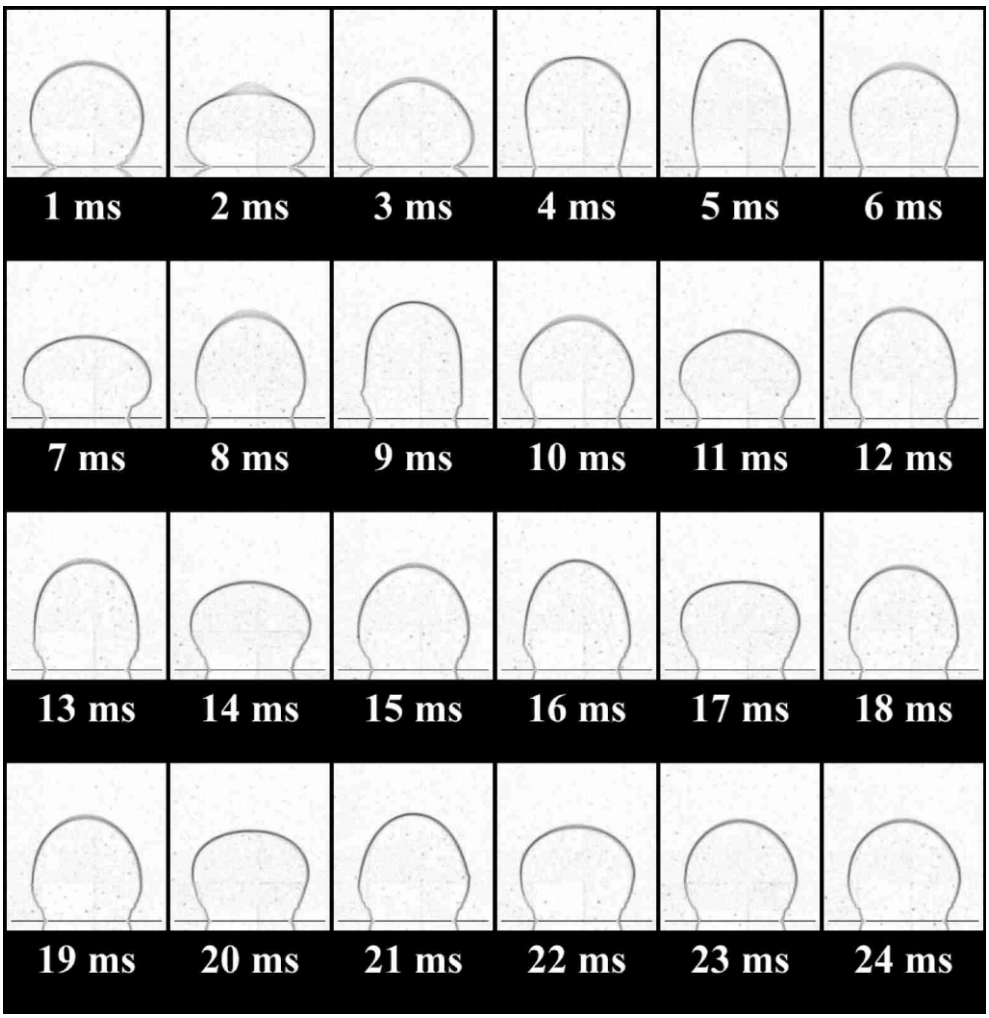

Fig. 5. Sequence of post-processed images of a molten solder droplet impacting on a smooth stainless steel substrate in reduced gravity. The reflection of the droplet from the substrate is visible in the bottom of all images. The horizontal line denotes the location of the substrate surface. The impact conditions are: $Re = 739$, $We = 1.282$, $Fr = 25{,}240$, $T_0 = 208°C$, $T_{sub} = 25°C$.

that the contact resistance between droplet and substrate increases markedly when solidification starts and the footprint of the droplet solidifies yielding a solid-to-solid interface.

When investigating the initiation of the freezing process, at the very beginning, period of strong oscillations in the solid-fraction can be observed, Fig. 9. During this period a repetitive solidification/remelting process occurs, the latter caused by the latent heat of the material. Whereas, the first nucleation of solid occurs, practically independent of the Froude number, at approximately the same dimensionless time (0.15), the duration of the above-mentioned remelting/freezing period (yielding fluctuations in the solid fraction) increases with increasing Froude (Fig. 9). It is possible that this phenomenon is due to the increased heat convection inside the droplet due to higher impact velocities as well as the larger freezing front corresponding to increased amounts of released latent heat at higher Froude numbers. Fig. 10 depicts the evolution of the height of the center of the droplet free surface for the following cases: $Fr = 5555.6$ and $Fr = 88{,}888.9$, respectively. It is clear that the higher Froude number leads to much more severe deformation of the droplet.

An order of magnitude estimate of the relevant time, transfer and energy scales yielded the following. The heat transfer coefficient for the liquid phase contacting the substrate is about an order of magnitude larger than the transfer coefficient for the solid–solid contact. The initial superheat energy, based on the baseline conditions given above, is about an order of magnitude smaller than the latent heat of fusion of the droplet

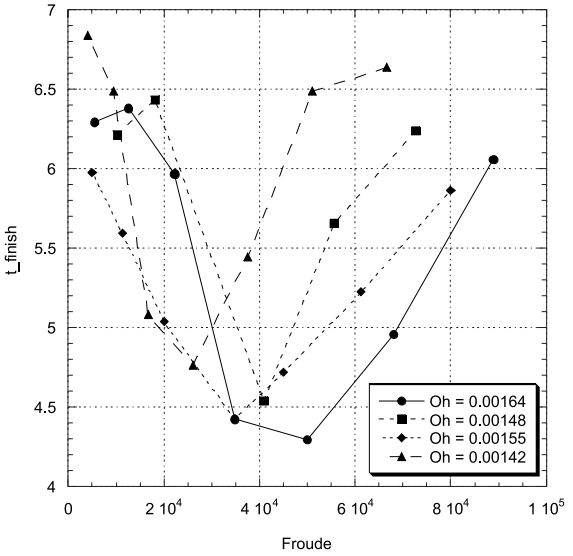

Fig. 6. The final dimensionless solidification times, t_{finish}, plotted against the Froude number, showing for groups of constant Ohnesorge number distinct minima in the solidification time depending on the Froude number.

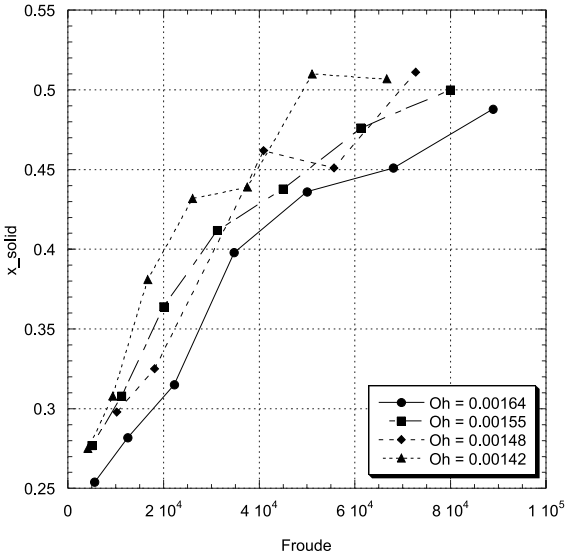

Fig. 7. Solidified radii, x_{solid}, of the contact area plotted against the Froude number for groups of constant Ohnesorge number.

material. The total solidification times are about an order of magnitude larger than the initial stages of the impact where simultaneous spreading and cooling as well as remelting take place. As seen in Fig. 11, the spreading occurs very fast and the final contact radius, x_{contact}, is attained before the remelting period is completed and continuous solidification occurs. Based on

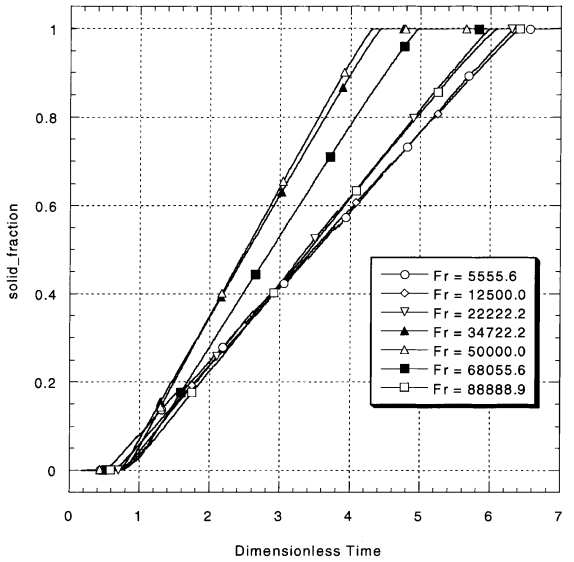

Fig. 8. Temporal evolution of the solid-fraction for $Oh = 0.00164$.

these estimates it can be assumed that most of the superheat energy is transferred to the substrate before stable solidification evolves. This assumption is corroborated by Fig. 12 showing the evolution of the average droplet temperature. All droplets have reached an average temperature close to the melting temperature at the start of the stable solidification process. The second cusp in the curves in Fig. 12 represents the end of solidification. Thereafter only conductive cooling of the solid droplet occurs.

For a small superheat energy compared to the latent heat of fusion, as is the case herein, convective removal of the superheat energy has presumably a small effect on the final solidification time. The final solidification times in the present study are dominated by the removal of the latent heat of fusion. As already mentioned above, the maximum spreading has already been attained when the stable bulk solidification is initiated. Since only little recoiling occurs thereafter, as can be seen in Fig. 11, the maximum spreading determines approximately the transfer area for the latent heat between the droplet and the substrate. The remaining energies in the droplet after initiation of the bulk solidification are about equal. The non-intuitive fact that the droplets with the largest contact area and Froude number/impact velocity do not solidify at the shortest time can be explained by the fact that bulk solidification in these droplets starts later, and more importantly, these droplets are more stretched and therefore feature a larger interface where heat is released. Simultaneously, the larger contact area with the substrate causes more heat to be removed.

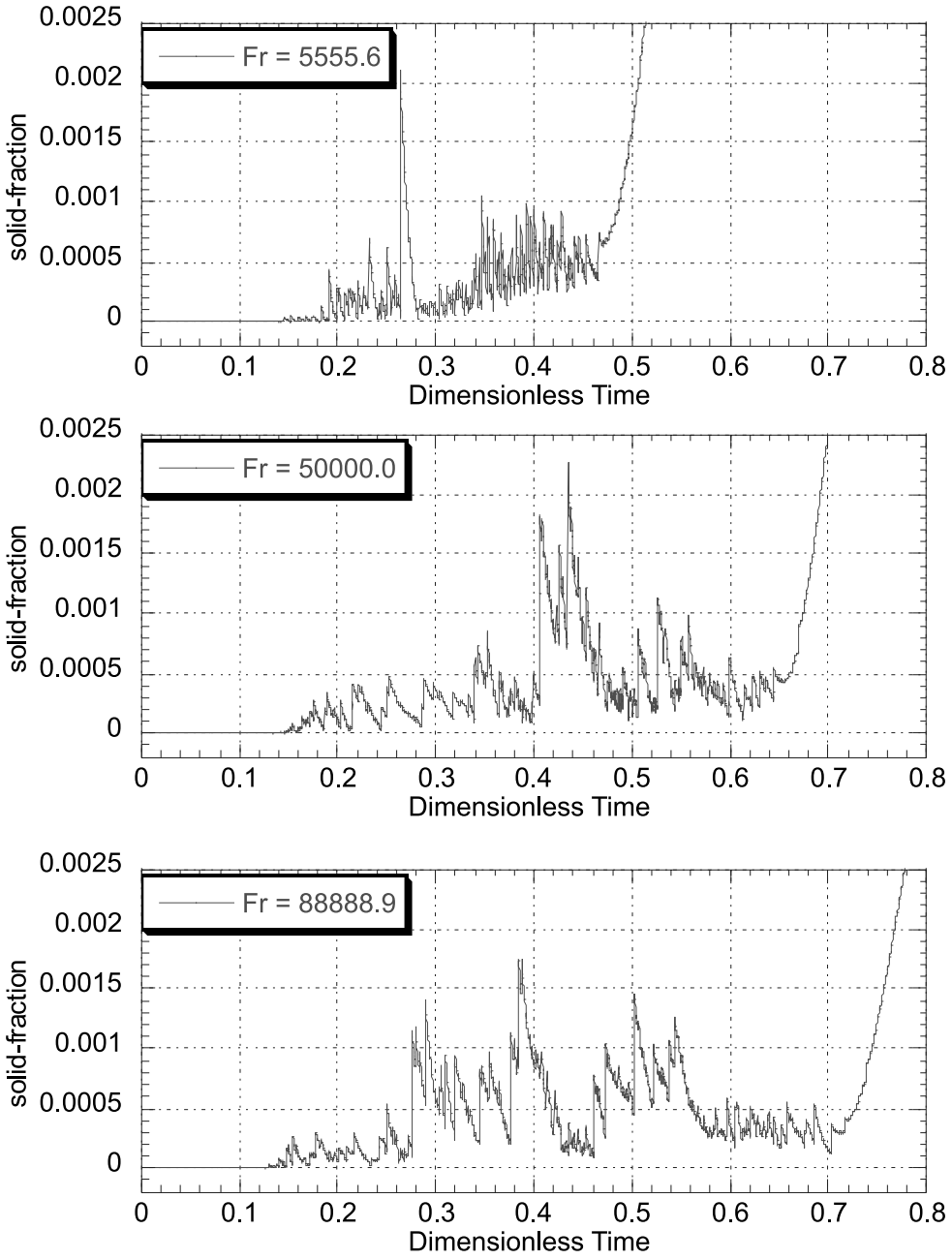

Fig. 9. Remelting period for three different cases at $Oh = 0.00164$.

4.5. Experimental results on the solidification during droplet impingement

As a comparison to the numerically obtained solidification times, shown for a set of four constant Ohnesorge numbers in Fig. 6, Fig. 13 presents solidification times for a number of experiments by Boomsma et al. [10]. The experimentally determined solidification times, t_{finish}, presented in Fig. 13 correspond to the experimental impact conditions as given in Table 4.

The two sets of experimentally determined solidification times correspond roughly to values of the Ohnesorge number of $Oh \sim 0.00142$ and $Oh \sim 0.00148$. Comparing the numerically obtained (Fig. 6) to the experimentally determined (Fig. 13) dimensionless solidi-

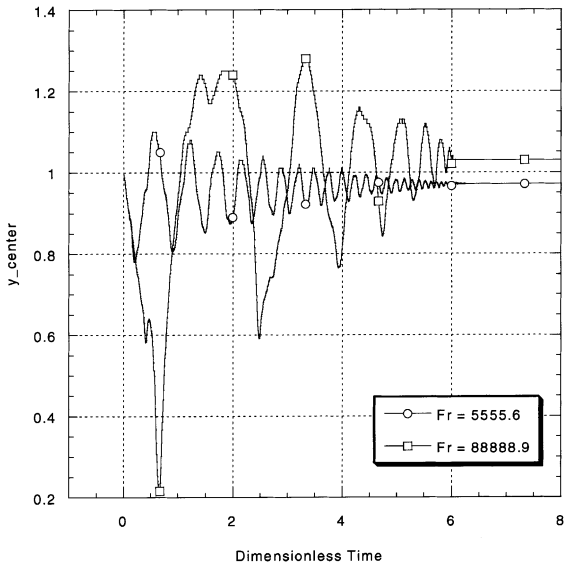

Fig. 10. Oscillations of the droplet top as a function of dimensionless time. Two cases at $Oh = 0.00164$.

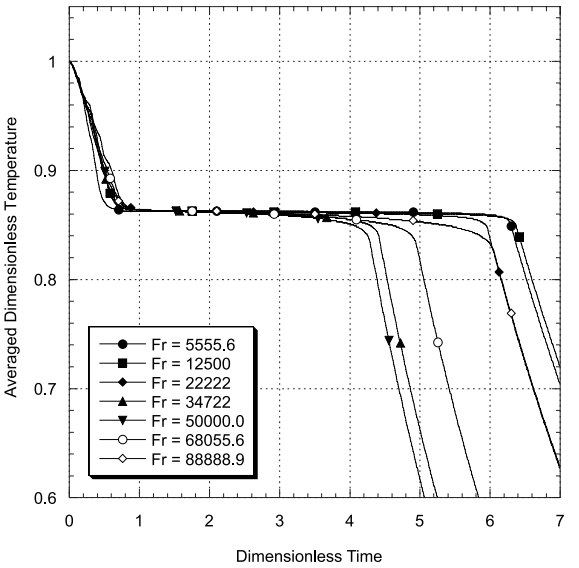

Fig. 12. Averaged dimensionless temperature of all droplets at $Oh = 0.00164$.

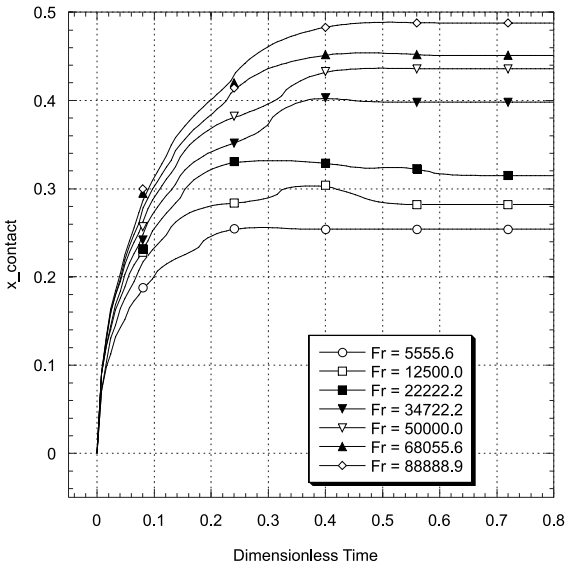

Fig. 11. Spreading history for all cases $Oh = 0.00164$.

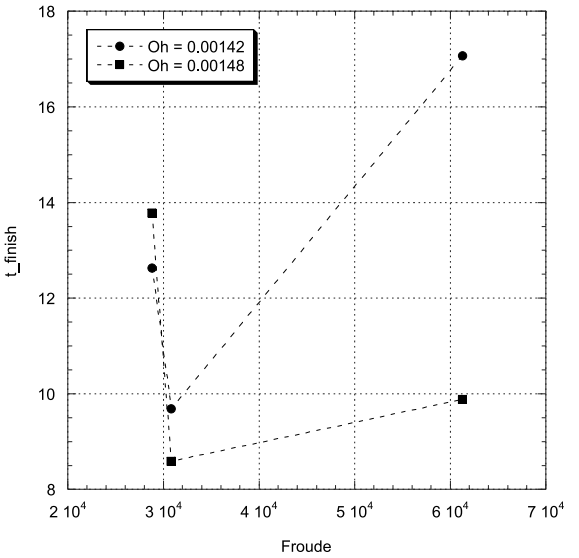

Fig. 13. Experimentally determined solidification times for two sets of approximately constant Ohnesorge numbers.

fication times, it is immediately obvious that the main finding of Fig. 6 (the existence of a minimum) is indeed verified.

On the other hand, it is worth clarifying that an accurate quantitative comparison of the absolute values of the experimental and numerical solidification times is not feasible. This is due to the fact that the experimental determination of the solidification times is somewhat intricate. It is based on the experimental visualization of the droplet impact sequences as described and shown in Boomsma et al. [10,12]. From the recorded impact sequences it was assumed that droplet solidification was accomplished when no fluid motion (e.g., droplet oscillations) was visible on the impact sequence recordings. The determination of this instant from the recorded sequences can be made within an accuracy of approximately six frames which gives an error of about ± 3 ms of the determined solidification time which in turn leads to a tentative error of the order of 10% in the dimensionless solidification times given in Table 4. Further-

Table 4
Impact conditions, corresponding dimensionless groups and final solidification times for the investigated experimental cases

Re	*We*	*Fr*	*Oh*	v_0 (m/s)	d_0 (m/s)	t_{finish} (ms)	t_{finish} (dimensionless)
1024	2.116	28,776	0.001396	0.27	1.24	58	12.63
991	2.024	30,798	0.001435	0.27	1.17	42	9.69
1410	4.075	61,260	0.001432	0.38	1.18	53	17.07
604	0.798	13,698	0.001479	0.17	1.11	90	13.78
1019	2.205	35,619	0.001457	0.28	1.14	35	8.59
1092	2.557	42,076	0.001464	0.31	1.13	36	9.38

more, this is only true if the visible fluid motion is arrested by solidification (likely) and not by viscous dissipation. Based on the above, the experimentally determined solidification times can only be considered as good estimates. Nevertheless, within the limitations stated above, the agreement between the solidification times from the simulations and the experiments is deemed as good.

5. Frozen shapes of droplets impacting in reduced gravity

The final shapes of the solidified droplets (in particular footprint and maximum height) are of interest to the industrial application of solder jetting. The cumulative effects of the influential parameters on the final shapes are shown in an array of increasing Froude and Ohnesorge numbers, respectively, in Fig. 14. A large number of ripples on the droplet surface is generated in reduced gravity due to rapid fluid oscillations in the presence of solidification. Furthermore, it is seen that the ripples are more pronounced (their amplitude increases) as the Froude number increases going from a "ball" shape to a "Christmas tree" shape. The latter shape features a desirable larger footprint, possibly leading to improved adhesion. The ball shape bumps for the lower Froude numbers, on the other hand, do not have a smooth surface. Their surface contains a multiplicity of small ripples, the presence of which is verified by the SEM picture in Fig. 3. As can be seen in Fig. 14 the frozen shapes of the droplets do not significantly depend on the Ohnesorge number. According to Schiaffino et al. [24] the investigated parameter range pertains to the case where the droplet impingement is impact driven. The dynamic spreading and the oscillations are primarily a result of the conversion interplay and between kinetic and free surface energies, hence the important influence of the Froude number that weighs the relative importance of impact kinetic energy and gravitation on the final bump shape. As can be seen in Fig. 10 the oscillations are damped by viscosity on a timescale which is long compared to the oscillation period and much longer than the spreading timescale. Therefore, the frozen shapes in Fig. 14 do not depend strongly on the Ohnesorge number. The realistic numerical prediction of these ripples (achieved in this work) underpins the need of accuracy in numerical simulations of the process.

6. Conclusions

In this paper, the main results of a study on the axisymmetric impingement of solidifying molten solder droplets onto smooth metallic substrates in a reduced gravity environment were presented. The study was mainly numerical and also included experimental verification, based on results of a companion experimental study. Millimeter-size droplet impact events in reduced gravity were employed for scale-up modeling of the impingement of picoliter size droplets of molten eutectic 63%Sn–37%Pb solder used in electronic chip packaging. In reduced gravity, the impact conditions correspond to $Re = \mathrm{O}(100)$, $We = \mathrm{O}(1)$, $Fr = \mathrm{O}(10{,}000)$, and $Ca = \mathrm{O}(0.001)$. One of the outcomes that stand out is the formation of a large number of frozen ripples on the droplet surface as a result of the simultaneous rapid fluid oscillations and solidification front advancement. Depending on the value of the Froude number, the shape of the final solidified microbumps range from ball to Christmas tree. The latter features a desirable larger foorprint which improves adhesion on the substrate. The ball shape bumps at the lower Froude numbers, do not have a smooth surface. Their surface contains a multiplicity of small-amplitude frozen ripples. A non-intuitive trend of the solidification times was also reported.To this end, the dependence of the final solidification time on Froude number (representing the variation of the impact velocity) was not monotonic and featured a distinct minimum for all values of Ohnesorge numbers in this study. Despite the complexity of the phenomena, the numerical model captures well the main features of the experimental results. In addition, it gives key insights on the influence of the Froude and Ohnesorge numbers on the evolution of the freezing process and the final solidified shape of the droplet.

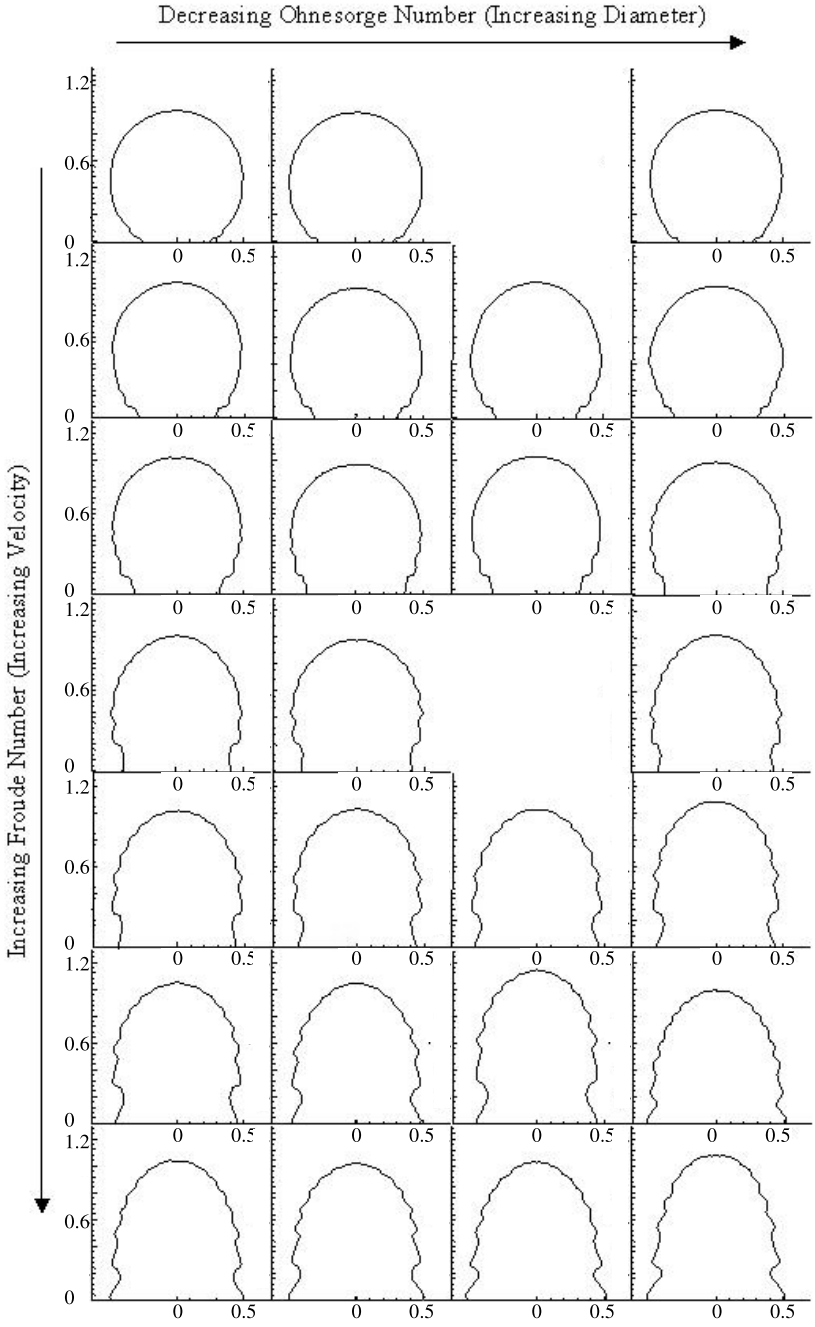

Fig. 14. Final solidified shapes of all cases given in Table 3.

Acknowledgements

The research reported in this paper was supported in part by NASA Grant NAG3-1905. The authors wish to acknowledge the personnel of the 2.2s drop tower of the NASA Glenn Research Center for their contributions during the performance of the reduced-gravity experiments. In addition, useful discussion with Dr. David Wallace of MicroFab Technologies is acknowledged with appreciation.

References

[1] J.W.S. Rayleigh, in: The Theory of Sound, Dover, New York, 1976.

[2] M.E. Orme, C. Huang, J. Courter, Precision droplet-based manufacturing and material synthesis, At. Sprays 6 (1996) 305–329.

[3] C.H. Amon, K.S. Schmaltz, R. Merz, F.B. Prinz, Numerical and experimental investigation of interface bonding via substrate remelting of an impinging molten metal droplet, ASME J. Heat Transfer 118 (1996) 164.

[4] D.J. Hayes, D.B. Wallace, M.T. Boldman, Picoliter solder droplet dispension, in: ISHM Symposium 92 Proceedings, 1992, pp. 316–321.

[5] D. Poulikakos, J. Waldvogel, Heat transfer and fluid dynamics in the process of spray deposition, Adv. Heat Transfer 28 (1996) 1–74.

[6] S. Haferl, Z. Zhao, J. Giannakouros, D. Attinger, D. Poulikakos, Transport phenomena in the impact of a molten droplet on a surface: macroscopic phenomenology and microscopic considerations, Part 1: fluid dynamics, in: C.-L. Tien (Ed.), Annual Review in Heat Transfer, vol. 11, Begell House, in press.

[7] D. Attinger, S. Haferl, Z. Zhao, D. Poulikakos, Transport phenomena in the impact of a molten droplet on a surface, Part 2: heat transfer and solidification, in: C.-L. Tien (Ed.), Annual Review in Heat Transfer, vol. 11, Begell House, in press.

[8] J.M. Waldvogel, D. Poulikakos, Solidification phenomena in picoliter size droplet deposition on a composite substrate, Int. J. Heat Mass Transfer 40 (1997) 295–309.

[9] B. Xiong, C.M. Megaridis, D. Poulikakos, H. Hoang, An investigation of key factors affecting solder microdroplet deposition, J. Heat Transfer 120 (1998) 259–270.

[10] K. Boomsma, C.M. Megaridis, D. Poulikakos, V. Nayagam, Contact angle dynamics of molten solder droplets impacting onto flat metallic substrates, Phys. Fluids, submitted.

[11] R.A. Granger, in: Fluid Mechanics, Dover, New York, 1995.

[12] K.S. Boomsma, Contact angle dynamics in molten metal droplet impact on flat substrates, Master Thesis in Mechanical Engineering, University of Illinois at Chicago, Chicago, 1999.

[13] C.W. Hirt, B.D. Nichols, Adding limited compressibility to incompressible hydrocodes, J. Comp. Phys. 34 (1980) 390–400.

[14] T.A. Baer, R.A. Cairncross, P.R. Schunk, R.R. Rao, P.A. Sackinger, A finite element method for free-surface flows of incompressible fluids in three dimensions, Part II: dynamic wetting lines, Int. J. Numer. Meth. Fluids, in press.

[15] W. Bushko, I.R. Grosse, New finite element method for multidimensional phase change heat transfer problems, Numer. Heat Transfer B 19 (1991) 31–48.

[16] J.M. Waldvogel, D. Poulikakos, D.B. Wallace, R. Marusak, Transport phenomena in picoliter size solder droplet dispension on composite substrate, J. Heat Transfer 118 (1996) 148–156.

[17] P. Bach, O. Hassager, An algorithm for the use of the Lagrangian specification in Newtonian fluid mechanics and applications to free-surface flow, J. Fluid Mech. 152 (1985) 173–190.

[18] X. Zhang, O.A. Basaran, Dynamic surface tension effects in impact of a drop with a solid surface, J. Colloid. Interface Sci. 187 (1997) 166–178.

[19] G.X. Wang, E.F. Matthys, Experimental investigation of interfacial thermal conductance for molten metal solidification on a substrate, J. Heat Transfer 118 (1996) 157–163.

[20] M. Pasandideh–Fard, R. Bhola, S. Chandra, J. Mostaghimi, Deposition of tin droplets on a steel plate: simulations and experiments, Int. J. Heat Mass Transfer 41 (1998) 2929–2945.

[21] W. Liu, G.X. Wang, E.F. Matthys, Thermal analysis and measurements for a molten metal drop impacting on a substrate, Int. J. Heat Mass Transfer 38 (1995) 1387–1395.

[22] T. Loulou, E.A. Artyukhin, J.P. Bardon, Estimation of thermal contact resistance during the first stages of metal solidification, Part I, Int. J. Heat Mass Transfer 42 (1999) 2119–2127.

[23] T. Loulou, E.A. Artyukhin, J.P. Bardon, Estimation of thermal contact resistance during the first stages of metal solidification, Part II, Int. J. Heat Mass Transfer 42 (1999) 2129–2142.

[24] S. Schiaffino, A.A. Sonin, Molten droplet deposition and solidification at low Weber numbers, Phys. Fluids 9 (1997) 3172–3187.